Digital Discovery

ROYAL SOCIETY OF CHEMISTRY

PAPER

View Article Online
View Journal

Check for updates

Cite this: DOI: 10.1039/d6dd00146g

A modular approach to studying polymer processing using a self-driving lab

Adedire D. Adesiji,[a] Dylan J. Balter,[a] Zhaoji Yang,[b] Kelsey L. Snapp,[d] Joseph M. Palomba[d] and Keith A. Brown*[abc]

Received 25th March 2026
Accepted 2nd June 2026

DOI: 10.1039/d6dd00146g

rsc.li/digitaldiscovery

Identifying processing conditions that yield optimal performance in polymer thin films remains challenging. Here we demonstrate a modular self-driving lab (SDL) for optimizing deposition conditions that produce strongly iridescent thin films. The platform combines a six-axis arm to move samples; a spray-coating station based on a re-engineered airbrush with independently actuated needle displacement, air-valve opening, and spray duration; an elliptical imaging station (EIS) that captures four viewing angles in a single image without moving components; and an indexer that sequentially positions wafers for automated transfer. To test this system, we maximized the iridescence of hydroxypropyl cellulose (HPC) thin films using Bayesian optimization. Within an experimental budget of 20 iterations, the SDL identified spray-coating parameters yielding the theoretical maximum iridescence of HPC on Si. Further analysis revealed that films thinner than ~290 nm exhibit optical behavior consistent with thin-film interference, whereas thicker films deviate from this trend at a thickness corresponding to the minimum cholesteric pitch of HPC, implicating additional contributions from cholesteric ordering. The functionality of the optimized films as signage and optically responsive humidity sensors was verified. This work establishes a modular framework for systematically mapping processing-structure–property relationships in thin-film deposition and autonomous exploration of polymer processing.

Introduction

Processing plays a key role in determining material structure and performance, yet identifying optimal processing conditions is a consistent challenge. This is particularly evident in the formation of polymer thin films, where small variations in deposition conditions can produce significant differences in the resulting film morphology. Among the deposition techniques, solution-based approaches such as spin coating, dip coating, and spray coating are widely used for fabricating polymer films due to their simplicity and compatibility with diverse deposition materials.[1,2] Spray coating is particularly attractive because it enables scalable deposition under ambient conditions across a wide range of substrates and integrates readily with roll-to-roll manufacturing.[3,4] However, the relationship between deposition parameters and resulting film properties is often complex due to the coupled dynamics of atomization, solvent evaporation, and film coalescence,[5,6] making it difficult to determine optimal processing conditions.

Self-driving labs (SDLs) address this challenge by combining automation and machine learning in a closed-loop framework that autonomously selects, executes, and analyzes experiments. Over the past decade, SDLs have emerged as a tool for accelerating materials research.[7–14] Several studies have demonstrated the effectiveness of SDLs, such as optimizing the stability of thin-film photovoltaics,[15,16] nanoparticle synthesis,[17,18] and catalytic activity of chemical compositions,[19,20] achieving faster convergence toward desired material performance than conventional experimental methods. However, despite the ability of SDLs to significantly accelerate materials discovery, their widespread adoption remains limited.[8,14,21] Many SDL platforms are built around rigid, workflow-specific architectures that rely on specialized robotic hardware and high-cost analytical instruments, limiting their adaptability to new experimental tasks.[22,23] For broader application of SDLs, there is a growing need for modular low-cost platforms that retain the accuracy and precision of more specialized equipment.

Most existing SDLs have focused on optimizing material synthesis and composition,[15,18,20,24–30] yet their application to polymer processing remains limited, even though processing conditions strongly influence structure and properties across multiple length scales. Rupnow *et al.* developed an SDL that optimized the spray-combustion synthesis of conductive palladium films, showing that closed-loop experimentation can effectively control complex deposition processes.[31] However,

---

[a] *Department of Mechanical Engineering, Boston University, Boston, MA, USA. E-mail: brownka@bu.edu*
[b] *Division of Materials Science & Engineering, Boston University, Boston, MA, USA*
[c] *Physics Department, Boston University, Boston, MA, USA*
[d] *Soldier Protection Directorate, U.S. Army Combat Capabilities Development Command Soldier Center, Natick, MA, USA*

SDLs have not yet been explored for polymer spray coating, where films form through physical deposition and solvent evaporation rather than reactive processes, directly linking deposition parameters to functional behavior.

In this work, we demonstrate a modular SDL for identifying spray conditions that produce strongly iridescent thin films. Iridescent thin films are technologically relevant due to their angle-dependent and tunable color response enabling applications in sensing,[32,33] photonic coatings,[34,35] and anti-counterfeiting.[36,37] The SDL platform includes a spray-coating station based on a re-engineered artisan airbrush equipped with actuators to precisely control needle position, air valve opening, and spray duration. Optical characterization is performed using the elliptical imaging station (EIS), which captures images from multiple angles simultaneously without motorized components. A 3D-printer-based indexer stores wafers and advances them sequentially to a fixed retrieval location for automated transfer. As a model system, we investigate hydroxypropyl cellulose (HPC), a biocompatible polymer whose iridescence arises from thin-film interference and cholesteric ordering, making it highly sensitive to processing conditions.[38,39] Within an active learning framework, the SDL tuned spray-coating parameters and identified conditions that reached the theoretical maximum iridescence strength in this three-dimensional parameter space with an experimental budget of 20 iterations. The optimal parameters were used to produce films that functioned as optically responsive humidity sensors and photonic signage. Collectively, this work extends the role of SDLs into polymer processing and demonstrates how modular, low-cost architectures can enable data-driven exploration of processing-structure–property relationships.

Results and discussion

To enable the optimization of iridescence in polymer spray coating, we developed a closed-loop workflow that integrates deposition, optical characterization, and algorithmic decision-making (Fig. 1). In each experimental cycle, the SDL performs spray coating by controlling the airbrush's needle position, air-valve opening, and spray duration to deposit polymer films under ambient conditions. The resulting films are then analyzed using the EIS to capture colors from multiple grazing angles θ, which can be used to characterize the iridescence strength of the film. These outcomes are fed into a Bayesian optimization algorithm using a Gaussian process regression model that determines the next spray-coating parameters to test. Through this iterative active learning process, the SDL rapidly establishes the relationship between processing parameters and film appearance, efficiently identifying conditions that yield strong iridescence.

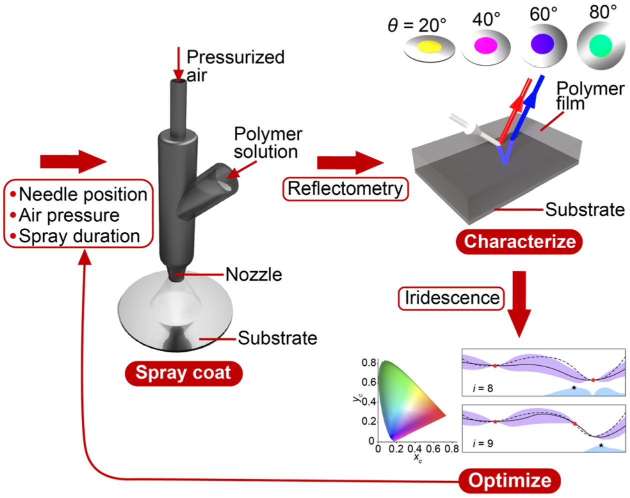

Fig. 1 Schematic of the polymer spray-coating self-driving lab (SDL) workflow. The SDL iteratively performs spray coating, characterization, and optimization in an active learning loop, where a machine learning model guides the selection of experiments to identify parameters that maximize film iridescence.

To enable rapid optical characterization of iridescent polymer films, the EIS was designed and constructed to capture multiple angles of a surface in a single photograph (Fig. 2). In addition to eliminating the need for moving parts, this design allows consistent lighting and imaging conditions to be applied to each angle for robust analysis. The design is based on the geometric property of an ellipse in which the sum of distances from any point M on the ellipse to its two foci F_1 and F_2 is constant, with each point M corresponding to a planar mirror positioned tangent to the ellipse, as expressed by

$$|MF_1| + |MF_2| = 2a \tag{1}$$

where a is the semi-major axis. This relationship indicates that light originating from one focus and reflecting from M will converge at the other focus with the same total optical path length (Fig. 2A). Consequently, all images of the sample seen by the camera remain simultaneously in focus, regardless of viewing angle.

Ray-tracing analysis was performed to determine the optimal mirror placement and ensure non-overlapping reflection paths (Fig. 2B). The constructed EIS used a semi-major axis a = 279 mm and a semi-minor axis b = 273 mm; values selected to provide a compact geometry while enabling a good range of accessible θ including 20°, 40°, 60°, and 80°. Mirror coordinates (x_m, y_m) were defined using the ellipse equation

$$\frac{x^2}{a^2} + \frac{y^2}{b^2} = 1. \tag{2}$$

Each mirror was oriented such that a light ray reflected from the sample at F_1 would converge to the camera positioned at F_2. The tangent to the ellipse at each mirror coordinate defines the mirror normal such that the incident and reflected rays satisfy the law of reflection, where the angle of incidence equals the angle of reflection relative to the normal of the mirror. Planar mirrors 50×50 mm^2 in size were mounted at these positions. Four mirrors were mounted to direct the incident light, and four additional mirrors were mounted to direct the light reflected off the sample to the camera. A Logitech Litra Glow was used to create a uniform diffuse light source at F_1. Images were

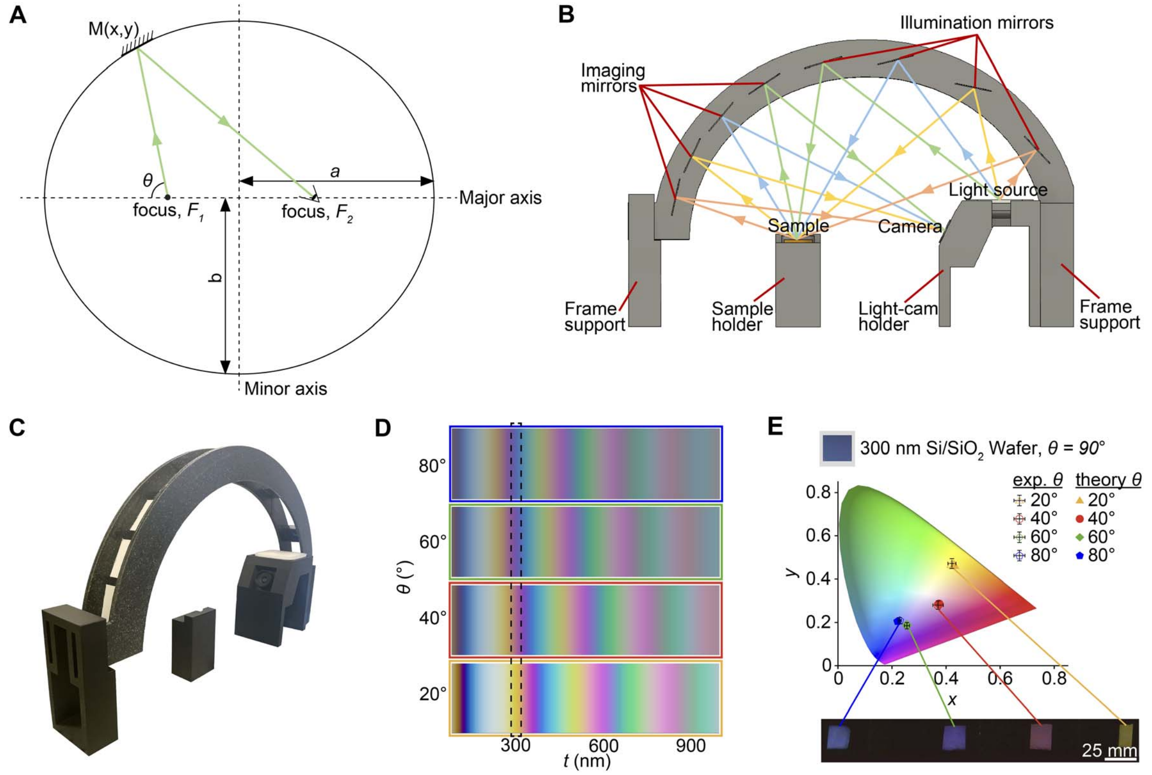

Fig. 2 Design and operation of the elliptical imaging station (EIS) for multi-angle optical characterization. (A) Schematic of the EIS operation principle. The ellipse, defined by semi-major and semi-minor axes *a* and *b*, has focal points F_1 and F_2. Light reflecting off *M* from one focus hits the other focus while traveling the same path. (B) Ray-tracing model showing mirror placement along the ellipse. Illumination mirrors direct white light from a source onto the sample positioned at F_1, while imaging mirrors collect the reflected light at distinct grazing angles $\theta = 20°$, 40°, 60° and 80° and direct it to the camera located at F_2. (C) Photograph of the EIS, featuring an arch for mirror placement and 3D-printed supports for the arch, sample, camera, and illumination source. (D) Simulated thin-film interference model for a Si/SiO_2 system, illustrating color variation with θ and oxide layer thickness *t*. (E) EIS image of a 300 nm thick SiO_2 film on Si wafer and corresponding CIE 1931 chromaticity plot with thin-film interference model predictions.

collected using a Mokose UC40M equipped with a 3.2 mm focal-length lens providing an 85° field of view. All mounting components, including supports for the camera, sample holder, light source, and the elliptical frame, were designed to interlock as a single assembly to maintain alignment (Fig. 2C). The elliptical arch was machined from black high-density polyethylene (HDPE) and the rest of the components were additively manufactured using fused filament fabrication out of polylactic acid (PLA). The entire assembly was enclosed within a black box fitted with a sliding door to block external light and undesired internal reflections.

To interpret changes in reflected color with viewing angle, we developed a theoretical thin-film interference model using the transfer-matrix method, incorporating the wavelength-dependent refractive indices and thicknesses of the constituent layers.[40] The computed reflectance spectra are then converted to perceptual color coordinates using the CIE 1931 standard observer under the D65 illuminant spectrum.[41] The CIE XYZ tristimulus values were then transformed to the sRGB color space for visualization. This model allows us to simulate any film, as shown in Fig. 2D for Si/SiO_2.[42]

As an evaluation of the EIS, we captured the iridescence of a 300 nm thick SiO_2 film on a Si wafer (Fig. 2E). The EIS image revealed distinct regions corresponding to different θ. Color data were extracted across each region, and mean chromaticity coordinates were calculated along with their standard deviations. The resulting chromaticity points, plotted with error bars on the CIE 1931 diagram, closely matched the values predicted by the model. This measurement validates the EIS as a platform to simultaneously capture light from four angles and also verifies the optical model developed to interpret EIS data.

To achieve reproducible and precisely tunable polymer film deposition, a spray-coating station was developed (Fig. 3). We modified an artisan airbrush, originally designed to be operated manually, that employs a mechanically coupled trigger mechanism in which needle displacement regulates liquid flow while simultaneously releasing pressurized air for atomization. Using motorized linear actuators, the needle displacement and the nozzle air release were separated and automated, with optical end stops integrated to provide consistent positional referencing for precise motion control. To control the degree of atomization, a motorized ball valve was incorporated, with the compressed air supply upstream of the valve set to a maximum pressure of 30 psi using a regulator. Altogether, this configuration enables independent control of flow rate through needle displacement, spray duration through nozzle actuation, and air

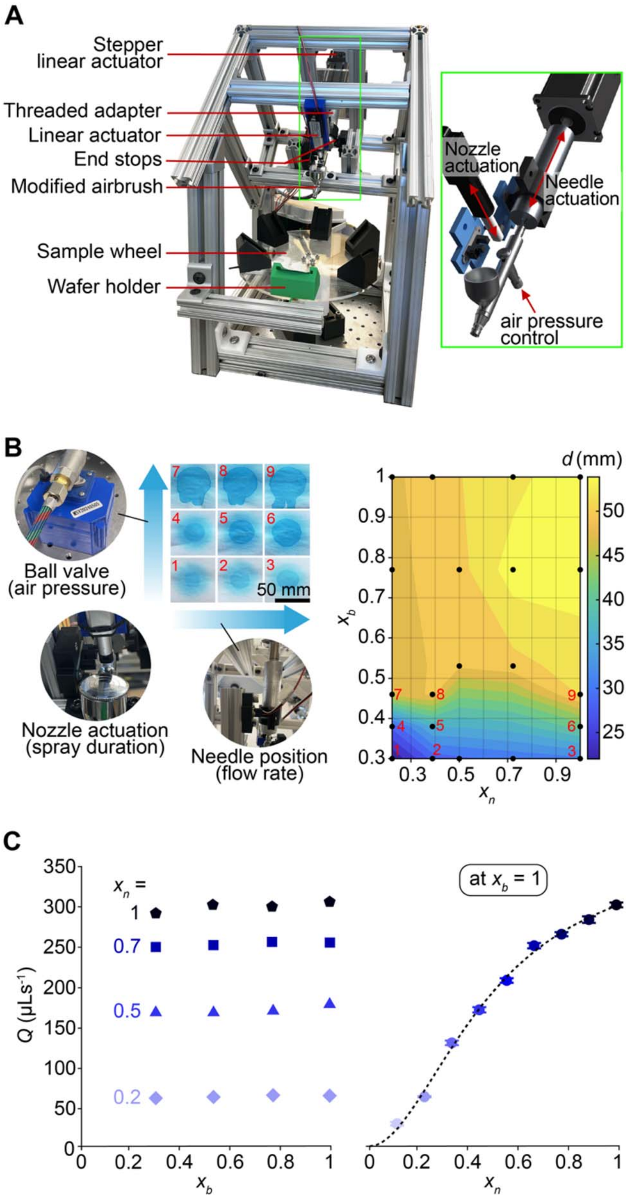

Fig. 3 Development and validation of the spray-coating station for controlled polymer deposition. (A) Photograph of the spray-coating station showing the airbrush assembly with motorized linear actuators for needle control and pressurized air release, actuator mounts with optical end stops, and a sample platform within an aluminum frame. Rendering of an isolated view of the nozzle and needle actuation mechanism and pressurized air inlet (right). (B) Evaluation of the spray parameters including the ball valve position x_b, nozzle actuation, and needle position x_n. Photographs show demonstrations of spray coating using food dye on white paper to illustrate how variations in x_b and x_n influence the resulting spray pattern diameter d. The contour map summarizes the complete dataset. (C) System validation measurements showing the nozzle flow rate Q at varying x_b with x_n values 0.2, 0.5, 0.7 and 1 (left), and Q as a function of x_n with $x_b = 1$ with data points representing triplicate measurements (right). Dashed lines show a sigmoidal fit to guide the eye.

pressure *via* the ball valve (Fig. 3A). The operation of the system is coordinated through an Arduino microcontroller. The airbrush is mounted at a 45° angle relative to the horizontal in a rigid extruded aluminum frame. This orientation aligns the fluid reservoir vertically to retain the maximum solution and prevent leakage through the nozzle. The sample substrate is positioned perpendicular to and 12 cm from the nozzle for uniform deposition.

Prior to using the spray-coating system for polymer deposition, it is necessary to quantify the role of the control parameters. Three controllable parameters define the spray-coating behavior: the ball valve position x_b, the needle position x_n, and the spray duration (Fig. 3B). While spray duration directly determines the amount of deposited material, the combined effects of x_b and x_n govern the spray cone geometry. To visualize these effects, FD & C blue 1 food dye was sprayed onto white paper for 3 s at various combinations of x_b and x_n, and the resulting diameter d of the spray pattern was measured for each sample. The results show that d increased with both increasing x_b and x_n. The most notable changes occurred at small x_b, where small adjustments led to measurable differences in d, indicating high control sensitivity in that regime. At higher x_b, the relationship becomes more gradual, providing more stable control over d. The resulting contour map of $d(x_b, x_n)$ shows that the spray geometry can be tuned continuously across this space (Fig. 3B).

To further quantitatively characterize and validate the spray system, the volumetric flow rate Q was measured as a function of both x_b and x_n using deionized water (Fig. 3C). For each trial, the mass of dispensed water collected over a 5 s spray duration was measured with a scale and converted to a volumetric flow rate. Across the range of x_b, Q varied only slightly at fixed x_n values of 0.2, 0.5, 0.7, and 1. Consequently, moderate changes in air pressure result in relatively small changes in flow rate due to the small aperture of the needle acting as the dominant resistance to flow. This indicates that the ball valve primarily influences droplet atomization rather than total volumetric flow. In contrast, when the valve was at fully open position, $x_b = 1$, the dependence of Q on x_n was measured in triplicate and followed a smooth monotonic relationship. Collectively, these results establish the spray-coating station as a robust platform that enables precise control over material deposition.

Following the validation of the spray-coating station and EIS, they were integrated with a sample indexer and robotic arm for sample transfer to enable an SDL workflow for optimizing film iridescence (Fig. 4A). The SDL operates as a fully coordinated system in which all modules are controlled by a central computer. The sample indexer is based on a 3D printer that was converted to enable sample transfer and storage, and it includes a 3D-printed cassette designed to hold twenty 50 mm diameter silicon wafers. The cassette is mounted on a repurposed MakerGear M3 printer with its motion bed programmed for automated wafer indexing. Following spray deposition and optical characterization, the robot returns the coated wafer to the storage section of the cassette, after which the bed advances the next wafer into the pickup position to begin the next cycle. This design eliminates the need for the robot to navigate multiple waypoints to find each sample, greatly simplifying motion planning and reducing positional errors compared to fixed cassettes. The modular, repurposed, and low-cost design

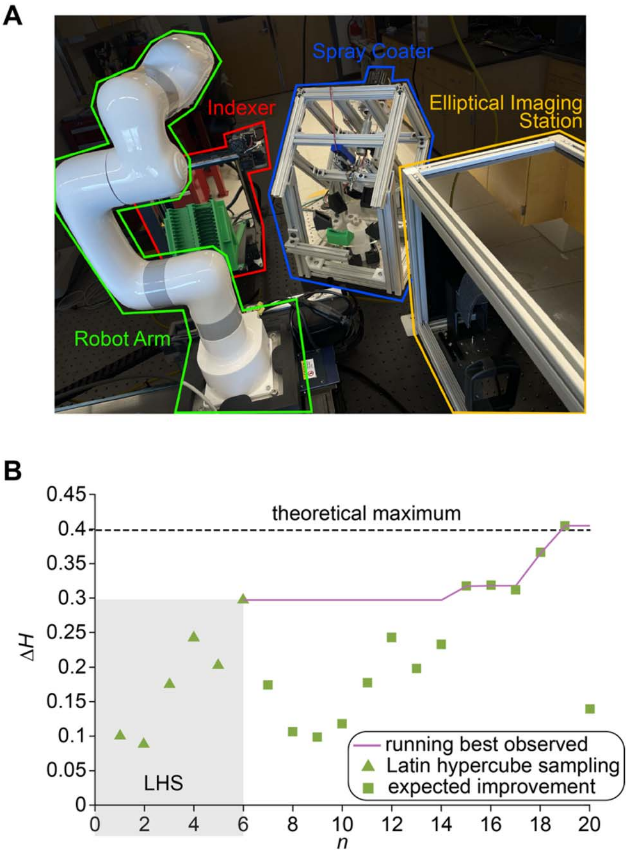

Fig. 4 Closed-loop optimization of film iridescence using the SDL. (A) Photograph of the complete SDL setup showing the robot arm, sample indexer, spray-coating station, and elliptical imaging station (EIS). Each module communicates with the control computer for autonomous experimentation. (B) The active-learning optimization process for the iridescence strength ΔH of hydroxypropyl cellulose (HPC) films with an experimental budget of 20 iterations. Six initial experiments were generated using a Latin hypercube sampling (LHS), while the remaining experiments were selected sequentially using Bayesian optimization.

demonstrates that SDL architectures can be adapted to other experimental workflows without specialized or expensive instrumentation.

In order to optimize the iridescence of polymer thin films, the SDL was operated in a closed-loop active-learning workflow (Fig. 4B). The system was tasked with maximizing the iridescence strength of hydroxypropyl cellulose (HPC) films deposited from a 1 wt% HPC solution in ethanol. HPC is a biopolymer whose reflected color arises from both thin-film interference and cholesteric ordering of its polymer chains.[38,39] As a result, it is highly sensitive to processing conditions, making the optimization landscape complex and nonlinear. The SDL experiments were performed under ambient laboratory conditions at approximately 45–50% relative humidity. To enable quantitative feedback, the iridescence strength of each film was evaluated from its CIE 1931 chromaticity coordinates (x, y) extracted from EIS images captured at four grazing angles ($\theta = 20°, 40°, 60°$, and $80°$). The chromaticity coordinates (x, y) describe color independent of luminance and were therefore used to quantify angular shifts in perceived hue. The Euclidean color distance between adjacent viewing angles was calculated as

$$d_{\theta_i-\theta_j} = \sqrt{\left(x_i - x_j\right)^2 + \left(y_i - y_j\right)^2} \quad (3)$$

and the iridescence strength ΔH was defined as the sum of these color shifts:

$$\Delta H = d_{20-40} + d_{40-60} + d_{60-80} \quad (4)$$

A higher ΔH value corresponds to a stronger color variation with viewing angles.

The optimization process was carried out over a limited experimental budget of 20 iterations to explore the design space defined by needle position, ball-valve opening, and spray duration. The first six experiments were selected using Latin hypercube sampling (LHS) to warm start the Bayesian optimization process by training the hyperparameters. After each spray-coating cycle, the resulting film was characterized using the EIS, and the resulting ΔH was fed into a Bayesian optimization algorithm based on a Gaussian process regression model. Bayesian optimization was performed using the built-in functions in MATLAB (The MathWorks Inc.) with a Matern 5/2 kernel without automatic relevance determination. Input variables were min–max normalized to the range [0, 1] prior to Gaussian process training and acquisition function evaluation. The model predicted the most promising experimental conditions by balancing exploration of uncertain regions and exploitation of high-performing areas using expected improvement as the acquisition function. Through this iterative, data-driven process, the SDL progressively learned the relationship between spray-coating parameters and the optical response of HPC, converging toward deposition conditions that produced strongly iridescent film (Fig. S2–S4). The implementation of the closed-loop workflow, including experiment orchestration and Bayesian optimization scripts, is provided in the code repository. The maximum ΔH achieved was 0.404 ± 0.012 (standard error of the mean from 9 sampling points); which was within error of the 0.397 theoretical limit predicted by the thin-film interference model for HPC films on Si, validating the effectiveness of this SDL in identifying optimal processing conditions.

To understand how the processing outcomes relate to optical response, we examined the dependence of ΔH on the thickness of the films produced from the optimization campaign (Fig. 5A). Thickness t was determined from the central 3×3 grid region of each wafer, corresponding to the same area analyzed for chromaticity in the EIS images. These values were extracted from thickness maps acquired using a Filmetrics F20 thin-film analyzer over a 7×7 grid centered on the wafer with 0.5 mm spacing between measurement points (Fig. S5). As shown in Fig. 5A, ΔH followed the trend predicted by the thin-film interference model up to ~290 nm, beyond which the experimental data deviates from the model prediction. This transition coincides with literature reporting the minimum cholesteric pitch of HPC to be ~280 nm,[43,44] which sets the minimum thickness required for the emergence of cholesteric ordering in

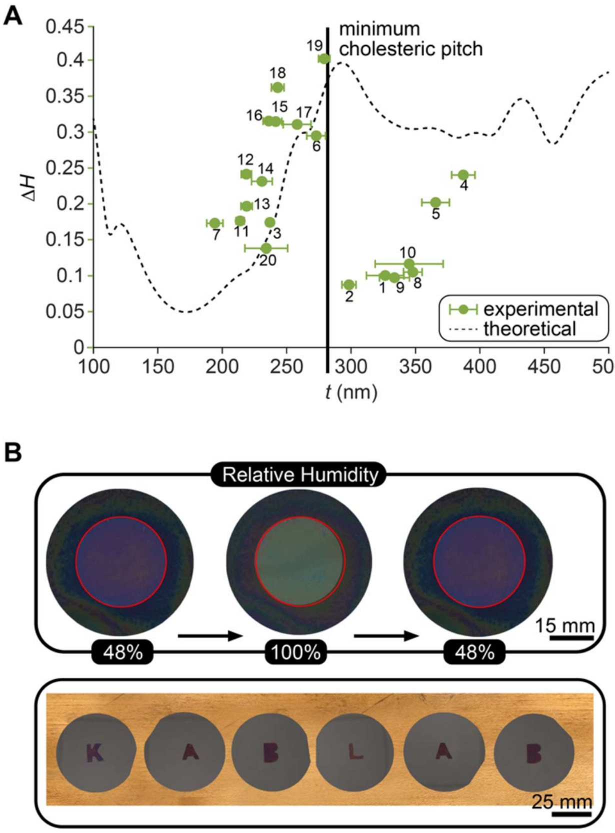

Fig. 5 (A) Iridescence strength ΔH of hydroxypropyl cellulose (HPC) as a function of film thickness t. Error bars represent the standard deviation of thickness measured over a central 3 × 3 region of each sample. Dashed line shows the minimum cholesteric pitch of HPC. (B) Functional demonstrations of optimized HPC films. Reversible optical response of a film under varying relative humidities (top). Films applied as patterned coatings to produce vivid lettering 'KABLAB' for signage applications (bottom).

HPC films. Beyond the minimum cholesteric pitch, iridescence is representative of the combined effects of thin-film interference and cholesteric structural coloration within the regime explored in this study. This deviation from the simple thin film interference model is further evidence of the importance of processing on the properties of polymer thin films.

Following the optimization of spray-coating, we sought to explore functional uses of the resulting HPC films. HPC exhibits vivid structural color determined by the film's optical path length, and since it is hygroscopic, changes in ambient humidity cause the film to absorb moisture and swell, altering its thickness and effective refractive index. This variation shifts the interference condition of the reflected light, producing a visible and reversible change in color. To explore this response, an optimized HPC film was first observed under ambient laboratory conditions at 48% relative humidity and then placed inside a sealed Petri dish saturated with water vapor at 100% relative humidity. The film exhibited a pronounced color shift upon hydration and returned to its original appearance re-equilibrated to room humidity (Fig. 5B, top). To illustrate the potential for signage applications, films were deposited on silicon wafers under the optimized spray-coating conditions and patterned using a stencil. The resulting lettering "KABLAB" demonstrated strong color contrast under ambient illumination (Fig. 5B, bottom). In the top and bottom images, $\theta \sim 90°$.

Conclusion

This work presents a modular SDL capable of spray coating polymer thin films and evaluating their iridescent properties. The platform automates a low-cost airbrush, introduces the simple and effective EIS for multi-angle optical characterization, and repurposes a 3D printer as a sample indexer. Operating together, these modules comprise a closed-loop system that enables precise and reproducible film deposition guided by real-time experimental feedback. Using hydroxypropyl cellulose (HPC) as a model system, this SDL efficiently identified spray-coating parameters that maximize iridescence strength within an experimental budget of only 20 iterations. Also, the experimental campaign achieved an iridescence strength reaching the theoretical maximum, demonstrating the efficiency of the optimization workflow. Notably, navigating this multidimensional processing space through conventional experimentation would require extensive manual iteration and is unlikely to systematically identify optimal conditions within a comparable timeframe. Further analysis revealed HPC exhibits regime-dependent optical behavior that cannot be fully predicted by thin-film interference model, highlighting the capability of an SDL to uncover emergent properties from varying processing conditions through the combination of iterative data-driven experiment selection and automation.

This SDL establishes a minimal approach for extending autonomous experimentation into polymer processing, an area traditionally guided by trial-and-error approaches and human intuition. This proof of concept shows that it is possible to construct a fully automated system to optimize spray-coating of polymers for functional properties. This validation justifies the use of this and related systems for the exploration of much larger parameter spaces that would require hundreds or thousands of experiments. Indeed, the added value of such an SDL is drastically amplified when considering larger parameter spaces as manual experimentation becomes fully impractical. Future work can include incorporating *in situ* thickness and spectral monitoring, multi-material deposition, and complex active learning strategies to explore more convoluted structure-processing-property relationships, advancing the broader goal of intelligent, data-driven materials development.

Author contributions

Conceptualization: K. A. B., A. D. A., J. M. P.; methodology: A. D. A., K. L. S.; investigation: A. D. A., Z. Y., D. J. B., K. L. S.; supervision: K. A. B., J. M. P.; writing – original draft: A. D. A., K. A. B.; writing – review & editing: all authors.

Conflicts of interest

There are no conflicts to declare.

Data availability

All data are present in the main text and supplementary information (SI). The CAD assemblies, thin-film interference modeling script and SDL software are available at: https://doi.org/10.5281/zenodo.18812450. Supplementary information: includes the wiring diagram of the spray-coating station, EIS images and thickness map of the spray-coated films, and plot of iridescence strength and thickness as a function of deposition parameters. See DOI: https://doi.org/10.1039/d6dd00146g.

Acknowledgements

K. A. B., A. D. A., and D. J. B. acknowledge support from the Army Research Office (W911NF-24-2-0197). K. A. B. and Z. Y. acknowledge support from the Army Research Office (W911NF-25-2-0074). This work was performed in part using the shared laboratories and instrumentation supported by the Boston University Photonics Center. A. D. A. acknowledges support from the Boston University Nanotechnology Innovation Center.

References

1 S. M. Becerra, H. Özbayraktar, E. Kilinc and J. C. Mauro, Stuck on Glass: A Review of Polymer and Polymer Nanoparticle Composite Coatings in Glass Technology, *Int. J. Ceram. Eng. Sci.*, 2026, **8**, e70043, DOI: 10.1002/ces2.70043.
2 C. Kan, C. Luo and Y. Hou, Scalable deposition and drying methods toward large-area monolithic perovskite/silicon tandem solar cells, *Energy Environ. Sci.*, 2026, **19**, 1101–1123, DOI: 10.1039/D5EE06772C.
3 B. Fotovvati, N. Namdari and A. Dehghanghadikolaei, On coating techniques for surface protection: A review, *J. Manuf. Mater. Process.*, 2019, **3**, 28, DOI: 10.3390/jmmp3010028.
4 J. Chen, *et al.*, Metal Nanowires for Flexible and Wearable Sensors: Synthesis, Processing, and Device Applications, *Adv. Sensor Res.*, 2026, **5**, e00164, DOI: 10.1002/adsr.202500164.
5 E. Boel, *et al.*, Unraveling particle formation: From single droplet drying to spray drying and electrospraying, *Pharmaceutics*, 2020, **12**, 625, DOI: 10.3390/pharmaceutics12070625.
6 H. Kaur, A. Thakur and R. C. Thakur, in. *Advanced Nanomaterials for Solution-Processed Flexible Optoelectronic Devices 74-102*, CRC Press, 2025.
7 A. Adesiji, J. Wang, C.-S. Kuo and K. A. Brown, Benchmarking Self-Driving Labs, *Digit. Discov.*, 2026, **5**, 14–27, DOI: 10.1039/D5DD00337G.
8 M. Abolhasani and E. Kumacheva, The rise of self-driving labs in chemical and materials sciences, *Nat. Synth.*, 2023, **2**, 483–492, DOI: 10.1038/s44160-022-00231-0.
9 G. Tom, *et al.*, Self-driving laboratories for chemistry and materials science, *Chem. Rev.*, 2024, **124**, 9633–9732, DOI: 10.1021/acs.chemrev.4c00055.
10 E. Stach, *et al.*, Autonomous experimentation systems for materials development: A community perspective, *Matter*, 2021, **4**, 2702–2726, DOI: 10.1016/j.matt.2021.06.036.
11 K. L. Snapp, *et al.*, Superlative mechanical energy absorbing efficiency discovered through self-driving lab-human partnership, *Nat. Commun.*, 2024, **15**, 4290, DOI: 10.1038/s41467-024-48534-4.
12 H. Quinn, *et al.*, PANDA: a self-driving lab for studying electrodeposited polymer films, *Mater. Horiz.*, 2024, **11**, 5331–5340, DOI: 10.1039/d4mh00797b.
13 Q. H. Liang, *et al.*, Benchmarking the performance of Bayesian optimization across multiple experimental materials science domains, *npj Comput. Mater.*, 2021, **7**(1), 188, DOI: 10.1038/s41524-021-00656-9.
14 R. B. Canty, *et al.*, Science acceleration and accessibility with self-driving labs, *Nat. Commun.*, 2025, **16**, 3856, DOI: 10.1038/s41467-025-59231-1.
15 D. N. Cakan, E. Oberholtz, K. Kaushal, S. P. Dunfield and D. P. Fenning, Bayesian optimization and prediction of the durability of triple-halide perovskite thin films under light and heat stressors, *Mater. Adv.*, 2025, **6**, 598–606, DOI: 10.1039/d4ma00747f.
16 S. Langner, *et al.*, Beyond Ternary OPV: High-Throughput Experimentation and Self-Driving Laboratories Optimize Multicomponent Systems, *Adv. Mater.*, 2020, **32**(14), 1907801, DOI: 10.1002/adma.201907801.
17 Y. B. Jiang, *et al.*, An artificial intelligence enabled chemical synthesis robot for exploration and optimization of nanomaterials, *Sci. Adv.*, 2022, **8**(40), eabo2626, DOI: 10.1126/sciadv.abo2626.
18 T. Y. Wu, *et al.*, Self-driving lab for the photochemical synthesis of plasmonic nanoparticles with targeted structural and optical properties, *Nat. Commun.*, 2025, **16**(1), 1473, DOI: 10.1038/s41467-025-56788-9.
19 E. Annevelink, *et al.*, AutoMat: Automated materials discovery for electrochemical systems, *MRS Bull.*, 2022, **47**, 1036–1044, DOI: 10.1557/s43577-022-00424-0.
20 B. Rohr, *et al.*, Benchmarking the acceleration of materials discovery by sequential learning, *Chem. Sci.*, 2020, **11**, 2696–2706, DOI: 10.1039/c9sc05999g.
21 A. V. Tobias and A. Wahab, Autonomous 'self-driving' laboratories: a review of technology and policy implications, *R. Soc. Open Sci.*, 2025, **12**, 250646, DOI: 10.1098/rsos.250646.
22 S. Lo, *et al.*, Review of low-cost self-driving laboratories in chemistry and materials science: the "frugal twin" concept, *Digit. Discov.*, 2024, **3**, 842–868, DOI: 10.1039/D3DD00223C.
23 S. Doloi, *et al.*, Democratizing self-driving labs: advances in low-cost 3D printing for laboratory automation, *Digit. Discov.*, 2025, **4**, 1685–1721, DOI: 10.1039/D4DD00411F.
24 F. Bateni, *et al.*, Smart Dope: A Self-Driving Fluidic Lab for Accelerated Development of Doped Perovskite Quantum Dots, *Adv. Energy Mater.*, 2024, **14**(1), 2302303, DOI: 10.1002/aenm.202470001.
25 S. Sadeghi, *et al.*, Autonomous nanomanufacturing of lead-free metal halide perovskite nanocrystals using a self-

driving fluidic lab, *Nanoscale*, 2024, **16**, 580–591, DOI: 10.1039/d3nr05034c.

26 E. Fatehi, M. Thadani, G. Birsan and R. W. Black, A Critical Evaluation of a Self-Driving Laboratory for the Optimization of Electrodeposited Earth-Abundant Mixed-Metal Oxide Catalysts for the Oxygen Evolution Reaction (OER). *arXiv*, 2023, preprint arXiv:2305.12541.

27 A. Dave, *et al.*, Autonomous optimization of non-aqueous Li-ion battery electrolytes via robotic experimentation and machine learning coupling, *Nat. Commun.*, 2022, **13**(1), 5454, DOI: 10.1038/s41467-022-32938-1.

28 C. K. H. Borg, *et al.*, Quantifying the performance of machine learning models in materials discovery, *Digit. Discov.*, 2023, **2**, 327–338, DOI: 10.1039/d2dd00113f.

29 H. Ros, M. Cook and D. Shorthouse, Efficient discovery of new medicine formulations using a semi-self-driven robotic formulator, *Digital Discovery*, 2024, **4**(8), 2263–2272, DOI: 10.1039/D5DD00171D.

30 A. Thelen, *et al.*, Sequential Bayesian optimization for accelerating the design of sodium metal battery nucleation layers, *J. Power Sources*, 2023, **581**, 233508, DOI: 10.1016/j.jpowsour.2023.233508.

31 C. C. Rupnow, *et al.*, A self-driving laboratory optimizes a scalable process for making functional coatings, *Cell Rep. Phys. Sci.*, 2023, **4**(5), 101411, DOI: 10.1016/j.xcrp.2023.101411.

32 J.-D. Liu, C. Du, Y.-J. Song and X.-Y. Du, Ultra-flexible and tough iridescent cellulose nanocrystal-hydrogel membrane towards sensing, actuating and thermal management, *Carbohydr. Polym.*, 2025, **368**, 124240, DOI: 10.1016/j.carbpol.2025.124240.

33 R. Vaz, *et al.*, Lab-on-leaf: Bioimprinted zein films and natural microfluidics for integrated photonic sensing, *Mater. Today Commun.*, 2026, 114858, DOI: 10.1016/j.mtcomm.2026.114858.

34 X. Li, *et al.*, Structural coloration of 3D irregular surfaces via spraying of liquid photonic crystals for iridescent effect and high colorfastness, *Colloids Surf. A Physicochem. Eng. Asp.*, 2025, **708**, 136004, DOI: 10.1016/j.colsurfa.2024.136004.

35 Y. Han, *et al.*, Large-area free-standing photonic crystal films with robust iridescent and reusability based on porous paper-based media, *Nano Res.*, 2026, **19**, 94908209, DOI: 10.26599/NR.2025.94908209.

36 S. Xia, *et al.*, Using a Functional Wool Keratin Photoresist to Build Iridescent and Fluorescent 3D Micro-Pattern for Dual-Mode Optical Anti-Counterfeiting, *Small*, 2025, **21**, 2502166, DOI: 10.1002/smll.202502166.

37 S. Li, *et al.*, All-biomass tunable CPL films based on cellulose nanocrystals and Taxus carbon dots for multimodal anti-counterfeiting and encryption, *Carbohydr. Polym.*, 2026, 124956, DOI: 10.1016/j.carbpol.2026.124956.

38 Z. Zhang and L. Shang, Self-Assembled Hydroxypropyl Celluloses With Structural Colors for Biomedical Applications, *Smart Mater. Med.*, 2025, **4**, e70004, DOI: 10.1002/smmd.70004.

39 R. S. Werbowyj and D. G. Gray, Optical properties of hydroxypropyl cellulose liquid crystals. I. Cholesteric pitch and polymer concentration, *Macromolecules*, 1984, **17**, 1512–1520, DOI: 10.1021/ma00138a016.

40 P. Yeh and M. Hendry, Optical waves in layered media, *Phys. Today*, 1990, **43**(1), 77–78, DOI: 10.1063/1.2810419.

41 J. Schanda, *Colorimetry: understanding the CIE system*, John Wiley & Sons, 2007.

42 M. N. Polyanskiy, Refractiveindex.info database of optical constants, *Sci. Data*, 2024, **11**, 94, DOI: 10.1038/s41597-023-02898-2.

43 L. Wang, *et al.*, Spontaneously assembled cellulose nanocrystal structural color films with tunable properties, *Sci. Rep.*, 2025, **15**, 28840, DOI: 10.1038/s41598-025-98994-x.

44 H. Ren, T. Balcerowski and A. G. Dumanli, Achieving a full color palette with thickness, temperature, and humidity in cholesteric hydroxypropyl cellulose, *Front. Photonics.*, 2023, **4**, 1134807, DOI: 10.3389/fphot.2023.1134807.